Time Resolved PIV for Space-Time Correlations in Hot Jets

Mark P. Wernet*
National Aeronautics and Space Administration
Glenn Research Center
Cleveland, OH USA

Temporally Resolved Particle Image Velocimetry (TR-PIV) is the newest and most exciting tool recently developed to support our continuing efforts to characterize and improve our understanding of the decay of turbulence in jet flows – a critical element for understanding the acoustic properties of the flow. A new TR-PIV system has been developed at the NASA Glenn Research Center which is capable of acquiring planar PIV image frame pairs at up to 25 kHz. The data reported here were collected at Mach numbers of 0.5 and 0.9 and at temperature ratios of 0.89 and 1.76. The field of view of the TR-PIV system covered 6 nozzle diameters along the lip line of the 50.8 mm diameter jet. The cold flow data at Mach 0.5 were compared with hotwire anemometry measurements in order to validate the new TR-PIV technique. The axial turbulence profiles measured across the shear layer using TR-PIV were thinner than those measured using hotwire anemometry and remained centered along the nozzle lip line. The collected TR-PIV data illustrate the differences in the single point statistical flow properties of cold and hot jet flows. The planar, time-resolved velocity records were then used to compute two-point space-time correlations of the flow at the Mach 0.9 flow condition. The TR-PIV results show that there are differences in the convective velocity and growth rate of the turbulent structures between cold and hot flows at the same Mach number.

Nomenclature

D	=	nozzle diameter
K	=	number of data record segments used in periodogram computation
M	=	length of periodogram data segments
R_{uu}	=	Space-Time correlation function
t	=	time coordinate
T	=	static temperature
T_∞	=	ambient temperature
u_i	=	reference velocity in the space-time correlation
u_j	=	shifted velocity in the space-time correlation
U_c	=	convection velocity
U_{id}	=	ideally expanded jet velocity
x	=	axial coordinate
y	=	radial coordinate
σ_u	=	standard deviation in the u-component of velocity
τ	=	time-lag in space-time correlation
ξ_x	=	axial coordinate spatial-lag in space-time correlation
ξ_y	=	radial coordinate spatial-lag in space-time correlation

I. Introduction

Digital Particle Image Velocimetry (DPIV) has developed into a production grade research tool, which has been used in a wide variety of applications. At the NASA Glenn Research Center, DPIV has been extensively used to characterize the first and second order statistical properties of both cold and hot jet flows from internally and externally mixed nozzles in the Nozzle Acoustic Test Rig (NATR)[1] and from simple and chevron equipped nozzles in the Small Hot Jet Acoustics Rig (SHJAR)[2]. These PIV measurements provide an extensive and accurate database of 1st and 2nd order statistics for validation of Computational AeroAcoustic codes (CAA). The accuracy of these aeroacoustic models is directly dependent on our ability to accurately characterize turbulent flow statistics. The Lighthill acoustic analogy yields a fourth order two-point space-time correlation, which has previously proved difficult or impossible to measure in hot flows.[3] The need for two-point space-time correlation measurements of hot

* Senior Research Engineer, Optical Instrumentation Technology and NDE Branch, Associate Fellow AIAA

jet flows is widely recognized in the aeroacoustic community, since it is the pathway for determining the noise source terms.[4] Use of traditional hotwire probes in these hot jet flow fields is precluded due to the compressibility effects and elevated temperatures. Hence, a non-intrusive means for measuring these multi-point flow field properties across the range of hot and cold jet flows is required.

There is a large collection of flow statistics data on cold jets, where space-time correlations have been performed to estimate turbulent length and time scales.[5,6] However, cold jet flow data are not directly applicable to hot jet flows. The available data on heated jets is much more sparse. Ahuja, et al. used LDV to obtain single-point turbulence measurements in hot subsonic jets.[7] The only previous application of planar velocimetry techniques to acquire space-time correlations in hot jet flows was demonstrated by Bridges & Wernet, 2003. PIV has been used to obtain space-time correlations in a water tunnel flow.[8] Multi-plane, stereo DPIV has also been used to obtain space-time correlations in a low speed, cold, lobed nozzle flow.[9]

DPIV is able to provide high spatial resolution velocity measurements through the use of high resolution cameras. The temporal resolution has been limited by laser repetition rate and camera framing rate. The temporal limitations have previously been overcome by using two independent PIV systems, so that the location and time delay between image acquisitions could be varied without restrictions.[2] The complexity and difficulty of implementing such a dual PIV system is daunting. MHz rate PIV measurements have also been previously demonstrated on nozzle flows using a pulse burst mode laser and high speed camera system.[10] While offering high temporal resolution and high spatial resolution (1280x1024 pixels) measurements, the short image sequence length (8 images) limited the information that could be gleaned from the measurements. Work continues on the extension of the pulse burst mode laser pulse width, which could increase the applicability of these MHz rate systems.[11] A kHz rate PIV system has recently been used to study the low frequency oscillations in shock induced turbulent separation.[12] In this work, the diode pumped Nd:YLF laser produced relatively long duration pulses, which in the high speed flow, yielded streaked particle images that decreased the accuracy of the velocity estimates. Commercial Temporally Resolved PIV systems are now available which support acquisition rates up to 1 kHz with laser pulse energies in the 20 mJ/pulse range. These systems are adequate for many non-stationary flows, but are incapable of providing relevant spectral properties of hot, turbulent jet flows.

A new Temporally Resolved PIV system has been developed and implemented at NASA GRC, which is capable of acquiring planes of flow measurements in supersonic jet flows at rates up to 50 kHz (frame pairs at 25 kHz) and time durations over 2 seconds, providing time records for computing spectral properties of the flow out to 12.5 kHz. The new TR-PIV system has been successfully applied to both hot and cold jet flows over a range of temperatures and Mach numbers in the SHJAR facility at NASA GRC. These measurements were obtained over an axial range of 0.5 to 12 diameters in both the shear layer and along the jet centerline. Measurements at the same Mach number for both cold and hot flows allows a direct comparison of the changes in the flow field properties. The cold flow measurements (T/T_∞ =0.89) obtained at Mach 0.5 using the new Time-Resolved PIV system are validated by comparison with previous hotwire anemometry measurements. Validating the TR-PIV measurements against well accepted hotwire results in the incompressible cold flow case ensures our confidence in the TR-PIV measurements in compressible, high temperature flows where hotwire measurements are not possible. The extensive time and spatial resolution of these measurements provides a new database of flow measurements previously unavailable. These flow measurements provide Lagrangian type measurements of the convective turbulent structures in the shear layer of an exhaust nozzle facilitating the computation of two-point space-time correlations. Two-point space-time correlation results for a Mach 0.9 flow case at both hot and cold conditions are presented illustrating the differences in the turbulent properties caused by temperature. This new database of flow measurements will be used to validate empirical correlations which predict the turbulent decay of the shear layer, a primary noise generation source. Examination of the actual two-point space-time correlations will guide the assumptions and flow models currently employed in aeroacoustic models.

II. Experimental Setup

II A. SHJAR Facility

The Small Hot Jet Acoustic Rig (SHJAR) is a single-stream hot jet rig that can cover the range of Mach numbers up to Mach 2, and static temperature ratios up to 2.8 using a hydrogen combustor and central air compressor facilities. For most testing, SHJAR uses a 50.8 mm diameter nozzle, but can operate larger nozzles with some limitation on cold setpoints at high Mach number. The SHJAR is located within the AeroAcoustic Propulsion Laboratory (AAPL)

at NASA's John H. Glenn Research Center. The AAPL is a 65 foot radius geodesic dome with its interior covered by sound absorbent wedges that provide the anechoic environment required to study propulsion noise from the several rigs that are located within. The jet rigs are positioned such that they exhaust out the open doorway, allowing the flows to be seeded with particulates and removing issues related to background noise from flow collectors. The nozzle being used in this test is one of a family of convergent nozzles, called the Simple Metal Chevron (SMC) nozzles, designed to be simple to characterize with similar dimensions such as inlet diameter (15.24mm), lip thickness (1.27mm), outside face angle (30° to jet axis), and parallel flow section at the exit (6.4mm). The facility has a 0.5m long settling chamber, which contains a series of screens located 18" upstream of the nozzle entrance to isolate the jet initial condition from small vagaries of the jet rig such as boundary layers. For this test, the SMC000 (no chevrons), with a diameter D=50.8 mm was used. Flow conditions from Mach 0.5 to 0.9 and temperature ratios of 0.89 and 2.7 were covered in the test matrix. The frequency fluctuations in the nozzle shear layer flows studied here are anticipated to be in the rage of 30-40 kHz for x/D >1 and on the order of 100 kHz close to the nozzle (x/D <1). Although the TR-PIV measurements only go out to 10 kHz and 25 kHz, the energy content in the flow drops by an order of magnitude over the range of 1 to 10 kHz, indicating that the major features (and most of the spectral energy) are captured by the TR-PIV measurements.

II B. Flow Seeding

For PIV, the fluid motion being measured is marked by the use of particles. These particles must be sufficiently small so they will have no slip relative to the fluid (so that their motion is the same as the fluid motion). In addition, all fluid must be laden with particles at a concentration high enough that sufficient particles (5-10) are found in an interrogation region of the recorded PIV images. In these tests we are mixing two fluids: the core stream and the ambient. It is also crucial that the seed be fully mixed and dispersed in the flow before the measurement region in order to assure good quality PIV images. Finally, the seed must not be affected by the high temperatures of the gas; this is especially true of the seed in the core stream at 520 C.

Two independent seeding systems were required in this study. The hot nozzle flow was seeded with a refractory seed material and the ambient air was seeded using a commercial 'smoke' generator. The refractory seed material used for the jet flow was 0.5 μm diameter alumina powder. A dispersion of the alumina seed material in ethanol was prepared using a pH stabilization technique.[13] The alumina/ethanol dispersion was dispersed in the flow well upstream of the nozzle using an air-assisted atomizing nozzle. The pH stabilization technique provides highly dispersed, unagglomerated seed particles in the flow. The ambient fluid was seeded with 0.3 μm mineral oil droplets produced by a commercial smoke generator. A large room circulation fan was used to disperse the concentrated smoke emitted by the smoke generator, providing a low velocity, uniformly seeded ambient air around the research jet.

II C. High Speed PIV System

Implementation of PIV measurement systems in the AAPL facility requires installation of the system on a large box beam traverse rig measuring 7x7x7 m in size, as seen in figure 1. This traverse has a range of roughly 2.5m along the jet axis with an accuracy of 1mm. The TR-PIV system implementation for this nozzle shear layer test represents an optimization of the available laser pulse energy and the flexibility afforded by the CMOS cameras to select a high aspect ratio region-of-interest at high framing rates. In order to achieve the objective of measuring a long spatial extent of the nozzle shear layer flow, the TR-PIV system was configured so that the laser light sheet propagated along the jet axis. By using a pair of CMOS cameras mounted side by side at the nozzle lip line height, the axial extent of the flow field being imaged was maximized. Forming the pulsed laser beam into a short height, thin laser light sheet ensured that there was sufficient energy density across the CMOS cameras' field of view so that the light scattered by the submicron sized seed particles in the flow could be detected. The laser head was mounted on a shelf on the right side of the rig and the laser power supplies were mounted on the floor next to the traverse, due to their large size and weight.

The CMOS cameras used in this study were Photron Ultima APX-RS cameras, which have 17.5 μm square pixels in a 1024x1024 pixel sensor. Each camera is capable of operating at 3000 fps at full resolution. Higher framing rates are available at reduced resolution. The primary objective of this test was to obtain Time Resolved PIV measurements of the flow at 10 kHz, with a secondary objective of 25 kHz measurements. In order to acquire "frame-straddle" image pairs at 10 kHz, the Photron cameras were operated at a framing rate of 20 kHz. In the remainder of the text, any reference to 10 kHz PIV implies that the cameras were operated at a frame rate of 20 kHz with the laser pulses synchronized to "frame straddle" the image frame pairs at 10 kHz. At 20 kHz, the sensor

region of interest was set to 144x1024 pixels. The combined dual camera configuration had a 144x2048 pixel field of view at 20 kHz. In the second test configuration for 25 kHz PIV, the cameras were set to acquire images at 50 kHz, with a resulting reduction in resolution to 80x640 pixels from each camera. The combined 25 kHz camera system had an effective field of view of 80x1280 pixels. The Photron APX-RS camera is a low noise design and has dynamic range of 10 bits, although only 8 bit image data was stored in these tests. The cameras were equipped with 85 mm focal length lenses with 1.4x teleconverters to obtain the desired 19 mm x 150 mm field of view from each camera at 20 kHz, or 10 mm x 94 mm at 50 kHz. The cameras were each equipped with 8 gigabytes of on board memory and a gigabit Ethernet interface for downloading the acquired image data. Each camera was connected to a separate PC to facilitate faster image downloads. Although the image acquisition time was slightly over 2.2 seconds at either frame rate, the image download time was typically 15-19 minutes/camera. The long download time is a limitation caused by a combination of the firmware used in the Photron cameras and the MS Windows operating system's inability to handle tens of thousands of files in a single directory. Registration of the camera images was obtained by aligning the camera fields of view with a ruler in the plane of the light sheet. The cameras were controlled by the 'FastCam' commercial software package provided by Photron.

The pulsed light sheet illumination was provided by a Quantronix Infini dual head laser system. The laser heads and beam combining optics are housed in a single enclosure. The Infini laser is flashlamp pumped and uses an RF driven Q-Switch to generate the 10 kHz pulses from each laser head. The nominal output pulse energy is 6 mJ/pulse/head at 10 kHz. The beam has an $M^2 < 16$ and the pulse length is 130 nsec at Full Width Half Maximum. When operated at 25 kHz, the pulse energies were nominally 2.5 mJ/pulse. The laser head is equipped with a remote shutter for turning off the laser output. The laser beam propagated downstream, parallel to the jet axis, to the light sheet forming optics as shown in figure 1. Pairs of cylindrical and spherical lenses were required in order to form the beam from the laser into a 20x2 mm light sheet at the measurement plane.

Two digital delay generators were used to control all of the system timing and synchronization. One delay generator was used to externally trigger the cameras, which needed to operate at 20 kHz in order to obtain image frame pairs at 10 kHz. The 20 kHz camera trigger signal was input into a second delay generator where it was used to synchronize the camera framing rate to the 10 kHz dual head laser pulse firing times. The cameras could have been used as a master time-base, however, during image saving operations the trigger output signal from the Photron cameras inverts in polarity and does not always provide a stable trigger source for the laser. Since laser failure can occur if a stable trigger signal is not supplied, the digital delay generator was used to provide continuous camera/laser timing signals.

The test matrix required measurements in both the shear layer and along the nozzle centerline in the potential core of the jet. Measuring the shear layer flow along the nozzle lip line necessitated propagating the laser light sheet from a downstream location back upstream to the nozzle exit. The light sheet was vertically centered on the nozzle lip line. The laser head was mounted so the beam propagated in a downstream direction. A 100x100 mm box beam was mounted on the large traverse to support the light sheet forming optics. The laser beam was turned 90° along the box beam, where the light sheet forming optics were mounted. The light sheet optics were enclosed in a sheet metal housing to protect them from the hot, seeded jet exhaust. A fused silica window was placed at the exit of the enclosure. A nitrogen purge stream of air was directed over the face of the exit window in order to keep it clear of seed material. In addition to the nitrogen purge, a right angle sheet metal wedge was fabricated to protect the exit window, see figure 2. The protective wedge had a slot cut out for the exiting laser beam and was flooded with 120 psi air to prevent seed material from entering the enclosure and coating the exit window. The laser beam propagated 2.1 m upstream from the sheet forming optics to the nozzle. For the measurements in the nozzle potential core, the light sheet generating optics and camera system were raised 25.4 mm and the laser beam propagated inside the nozzle.

Figure 2 shows the TR-PIV system in operation. The dual PIV computer systems were remotely located during data acquisition and controlled the CMOS cameras via their gigabit Ethernet interface. The dual TR-PIV camera system had an axial stream view against a black velvet covered background. The SHJAR is an outdoor facility, which typically dictates operation after sunset in order to avoid background contamination by sunlight. However, due to the short exposure intervals when operating the CMOS cameras at 20 kHz or 50 kHz, measurements were obtained in full daylight conditions, without interference filters.

III. Data Analysis

III A. PIV Image Processing

The collected TR-PIV image data were processed using an in-house developed PIV cross-correlation processing program called PIVPROC.[14] The correlation based processing software program supports subregion image shifting and multi-pass correlation in order to improve the spatial resolution of the resultant velocity vector maps. In addition, PIVPROC also supports subregion distortion processing[15], which proved to be critical in reducing the acquired image data. In multipass-correlation mode, the correlation processing grid is initially coarse (typically 64x64 pixel subregions), followed by a higher resolution 2nd pass (typically 32x32 pixel subregions) in order to improve the spatial resolution of the resulting vector field. The objective of the multi-pass approach is to keep the correlation peak at the center of the correlation plane, which mitigates higher order errors in the correlation peak detection process.[16] In each pass, PIVPROC uses a spurious peak removal algorithm which removes any vector lying more than 3σ from its surrounding 8 neighbors and replaces it with an interpolated value. The estimates for the subregion offsets used in each pass are computed from the previous pass vector map. The offsets are computed from a spatially weighted average of the vector field. PIVPROC uses a simulated annealing approach in the 2nd pass of the multi-pass correlation operation. For example, the first pass correlations may be performed at 64x64 pixel resolution followed by 2nd pass operations at 32x32 pixel subregions. In PIVPROC, a total of 6 passes at the higher grid density can be used, where in each successive pass the region on the correlation plane that is examined for correlation peaks is reduced. In the 6th pass, the correlation plane search region may only be 1/3 of the initial size. Since the subregion image shifting keeps the correlation peak at the center of the correlation plane, this simulated annealing approach reduces the number of spurious vectors by limiting where on the correlation plane the correlation peaks can be detected. The subregion offsets are computed from the surrounding flow field, so the local flow is directing the correlation operation on where to find the correlation peak. In addition to multi-pass correlation processing, PIVPROC also employs subregion distortion. Subregion distortion is used to correct for velocity gradients across the subregion and to minimize the "peak-locking effect, which is the tendency for the estimated particle displacements to preferentially concentrate at integer values. In the subregion distortion technique, the local velocity gradients surrounding the current correlation subregion are used to distort the subregion before the cross-correlation processing operation. Distorting the subregion yields correlation subregions with uniform particle displacements, and hence, reduces any bias caused by the velocity gradients. Typically two additional passes after the multi-pass processing are used with subregion distortion turned on to refine the correlation peak estimates. A high quality vector map (no spurious vectors) is required before using subregion distortion in order to not bias the resulting velocity field.

For the 10 kHz PIV images (1024x144 pixels), a first pass subregion size of 64x32 pixels was used, with 50% overlap, followed by 6 passes using 32x32 pixel subregions again with 50% overlap. When enabled, two additional passes were computed with subregion distortion operations. Hence, a total of 9 correlation passes were used on each data set. The resulting spatial resolution of the velocity vector grid was 0.05 D or 2.5 mm. At each measurement point, a total of 21845 image frame pairs were collected, per camera. Each measurement station in the flow survey contained 16 Gigabytes of image data (8 GB/camera).

For the 25 kHz PIV images (1024x80 pixels), the subregion size and processing grid resolutions were the same as those used in the 10 kHz data processing. Subregion distortion processing was also employed, yielding a total of 9 correlation passes on each data set. The resulting spatial resolution of the velocity vector grid was 0.05 D or 2.5 mm. At each measurement point, a total of 61440 image frame pairs were collected, per camera.

The computed vector maps from each camera were then merged into a single velocity vector map, where the processing grids in each of the camera images was shifted to ensure proper meshing of the combined vector maps. Typically 5 grid points from each camera's individual vector map overlapped in the combined vector maps. The processed, merged velocity vector maps were then ensemble averaged while imposing hard velocity cutoff limits and Chauvenet's Criterion to remove statistical outliers from the time sequence records[17]. Any identified outliers were flagged so that they could be replaced in subsequent time domain processing. The sequence of velocity vector maps were then converted from planar spatial data to a 2-D spatial grid of time series measurements and written to a single time record file.

III B. Spectral Computations

The time record file was read into the spectral processing program. Any data points that had been flagged in the spatial ensemble average processing (via hard velocity cutoff limits or the Chauvenet's Criteria) were replaced by interpolating across the missing point in the forward and backward time steps. Hence, spurious vectors identified in the ensemble average processing were replaced by a time-wise interpolated value. Replacement of any missing velocity vectors was required in order to ensure that a continuous time record was input to the spectral computation algorithm. Less than 1% of the vectors at any given grid point were replaced via temporal interpolation. Tests confirmed that vector replacements "in time" never exceeded more than one time step.

The ensemble averaged mean values of the reconstructed velocity time records were then computed at each grid point in the vector maps and subtracted from the velocity records to produce zero-mean velocity records. Spectral periodograms were then computed from the 21845 point (10 kHz) time records and the 61440 (25 kHz) time records. The periodograms were computed using 50% overlap and Welch windowing, in order to minimize the variance in the resulting periodograms. Assuming a total record length of $2 \cdot K \cdot M$ (where the total record is divided up into K segments of length $2M$ each), then by using 50% overlapping records the variance in the Power Spectral Density (PSD) estimate is reduced by the factor $9K/11$.[18] For the results presented below, the 25 kHz (61440 point time records) were processed using 1024 periodograms, and the 10 kHz (21845 point time records) were processed using 512 point periodograms, to ensure that the energy per frequency band was approximately equal. For the 25 kHz data records, K=60 data segments were averaged in the resulting periodograms, yielding power spectral density (PSD) estimates with a standard deviation of 14%. For the 10 kHz data records, K=42 data segments were averaged in the computation of the periodograms, yielding PSD estimates with a standard deviation of 17%.

III C. Hotwire Data

The Hotwire data were collected using a Dantec model 55p11 with a 5 μm diameter, 1.25mm long Platinum-plated tungsten wire. The hotwire was operated at an overheat of 0.6 and was controlled by a Dantec Streamline 90C10 module. The hotwire signal was digitized at 10 kHz and 16 bits resolution using an RC Electronics Datamax Digital Recorder. A 4 kHz anti-alias filter was used to filter the hotwire signal before it was digitized and stored. The 8 second long, 80,000 point hotwire time records were converted to zero mean flow records and 512 point periodograms were computed using Welch windows. A total of K=78 data segments were averaged together in the computed periodograms, producing PSD estimates with a standard deviation of 13%. The hotwire data were acquired several years previous to the current work with the objective of accurately characterizing the spread of the shear layer as a function of axial position. The conservative anti-alias filtering used to acquire the hotwire data may have removed too much of the high frequency content of the signal near the nozzle and therefore possibly under estimates the true turbulence intensity along the lip line near the nozzle exit. For range x/D > 1 the frequency content in the signals has dropped off significantly so that the hotwire turbulence estimates are more realistic.

IV D. Two-Point Statistics

Our motivation for developing Temporally Resolved PIV is driven by acoustic theory, which requires knowledge of the two-point space time correlations of the velocity field. TR-PIV yields time records of velocity across a planar grid of measurement points, which directly lends itself to the computation of two-point space time statistics. The processed time record/vector maps were then processed to compute the two-point spatial-temporal correlations via:

$$R_{ij}(\vec{\xi}, t, \vec{x}) = \frac{\overline{u_i(\vec{x} + \vec{\xi}/2, t) u_j(\vec{x} - \vec{\xi}/2, t + \tau)}}{\sqrt{u_i^2 u_j^2}} \qquad (1)$$

where $\vec{\xi}$ is the spatial lag variable and τ is the time lag variable in the correlation computation about the spatial point $\vec{x}$. The correlation has been normalized here by the reference variances: $\sqrt{u_i^2 u_j^2}$. The space time correlation R_{ij} can then be used to compute the spatial and temporal length scales of the flow.

IV. Results & Discussion

IV A. Ensemble Averaged Results

TR-PIV data were collected at both 10 kHz and 25 kHz in the Small Hot Jet Acoustic Rig fitted with the SMC000 50.8 mm diameter nozzle. Data were collected over a range of Mach numbers (0.5-0.9) and temperature ratios (T/T_∞=0.89 to 2.7). In addition, we have previous hotwire survey measurements from the SMC000 nozzle flow at Mach 0.5, which were used as a baseline case for validating the TR-PIV measurements. Figure 3 shows the SMC000 50.8 mm diameter nozzle and an instantaneous velocity vector map acquired at 10 kHz in order to give proper perspective of the TR-PIV system field of view, spatial resolution and the location of the measurements relative to the nozzle. The vector field shown here is the result of merging the left and right camera processed vector maps. Both high speed packets of fluid from the nozzle core flow and low speed fluid packets from the ambient are observed in the instantaneous vector field.

As a part of the ensemble averaging process, a data file is generated which contains the velocity along the lip line of the nozzle for the entire time record. Using this lip line data set, the velocity as a function of time and space can be plotted as shown in figures 4a and 4b. Figure 4a shows color contours of the u-component of velocity for the 10 kHz data set plotted as a function of x/D vs. Time and figure 4b shows the same information for a 25 kHz data set. The plots clearly illustrate the advection of a roughly equal number of low and high speed fluid packets downstream from the nozzle. The slope of the correlated fluid packets is proportional to the convective velocity, and is approximately 105 m/s. The time duration of the two plots is the same (15 milliseconds); however, the x/D ranges are different which causes the difference in the slope of the convection streamlines. The 25 kHz streamlines are more clearly resolved owing to the higher sampling frequency used in this case, especially in the region near the nozzle exit.

The "quality" of the ensemble averaged data sets is determined by examining the number of good velocity measurements at each grid point in the velocity vector map. Spurious velocity vectors are removed during the ensemble averaging process as described above. The data quality is defined as the number of good data points at each grid point relative to the total number of measurements in the ensemble. High data quality is typically obtained via a uniformly dispersed, high concentration flow seeding.

Ensemble averages of the 10 kHz and 25 kHz data sets were computed in order to evaluate the flow field properties and ensure accurate processing of the data. Several different processing strategies were applied to the TR-PIV image data. In many cases, the first and second order statistics do not reveal any discernable abnormalities in the data. In the end, the spectral properties of the processed data records yielded the strictest evaluation of the flow field properties. More details of the spectral properties of the TR-PIV measurements will be discussed in the next section. For the 10 kHz data set at Mach 0.5, the laser light sheet was not propagating perfectly horizontally. Instead it had a slight upward slope that caused the bottom edge of the light sheet to be above the bottom edge of the camera field of view close to the nozzle. The ambient air was seeded with a smoke generator which can at times provide a very dense scattering cloud. The interface at the edge of the light sheet results in a very sharp bright to dark transition in these PIV images. Figure 5 shows the mean velocity, turbulence intensity and data "quality" resulting from standard PIV processing: 64x32 pixel subregions on a 32x16 pixel grid followed by 6 passes using 32x32 pixel subregions on a 16x16 pixel grid. The mean velocity field appears unremarkable, the bottom edge of the high speed nozzle core is observed at the top of the flow field and the entrainment of low speed ambient air is observed at the bottom edge of the flow field. The relative standard deviation in the u-component of velocity is defined here as σ_u/U_{id}, where U_{id} is the ideally expanded jet velocity computed using the plenum pressure. The relative standard deviations shown here are quite high throughout the entire flow field. Axial turbulence intensities of approximately 20% are observed at an x/D of 1, which is approximately 1.6 times the expected value, based on hotwire measurements at this axial location. The data quality shows a moderate data dropout (quality of 92%) at the lower left region of the flow field, corresponding to edge of the light sheet illumination. It is unsettling to note that the mean flow field exhibits no peculiarities, even though there are substantial issues with the 2nd order flow statistics.

In order to mitigate the effects of the light sheet edge in the resultant velocity field, the Symmetric Phase Only Filtering technique was applied in the data processing.[19] Use of the SPOF technique dramatically improves the quality of the resultant velocity field. Note that in subsequent TR-PIV image acquisitions, the light sheet was modified to propagate horizontally through both camera fields of view, thereby eliminating this issue altogether. In addition to the SPOF processing, subregion distortion was also applied to improve the turbulence intensity estimates.

Figure 6 shows the 10 kHz flow field measurement results with the addition of the SPOF and subregion distortion data processing operations. The mean velocity field remains essentially unchanged from the result shown in figure 5, with a slight thinning of the shear layer and a more gradual velocity gradient across the shear layer. The axial turbulence intensities have now dropped across the entire flow field. Axial turbulence intensities of approximately 12% are observed at an x/D of 1, which exactly match the hotwire measurements at this axial location. The data quality is now better than 98% throughout the entire flow field, indicating that the SPOF processing has minimized the hard edge effect of the laser light sheet. It is also interesting to note that the output of the standard processing (the data shown in figure 5) is the input into the distortion processing stage (2 additional iterations of subregion distortion processing), which yields a significant reduction in the turbulence levels. Although the inclusion of the subregion distortion processing and the SPOF has improved the quality of the turbulence estimates throughout much of the flow field, the values in the shear layer at x/D=0.5 are slightly higher than expected. The higher turbulence in this region is attributed to the large velocity gradients, which can bias the velocity estimates depending on the magnitude of the gradient relative to the size of the correlation subregion. Further downstream, x/D > 0.7, the subregion distortion technique is able to correct for the large velocity gradients and the turbulence levels are in agreement with the hotwire results.

Figure 7 shows the 25 kHz PIV data results overlaid on top of the 10 kHz results. The data shown here were processed using the subregion distortion technique, which also yielded the best data set for the 10 kHz case. The black box denotes the outside boundary of the 25 kHz data sets. Overlaying the data sets for the 10 and 25 kHz cases illustrates the trade off in field-of-view in order to obtain higher temporal resolution. The 25 kHz data were collected starting at the same x/D = 0.5 location as the 10 kHz data, but extend only 4 diameters downstream. The mean flow and properties are very similar to the optimized data processing case for the 10 kHz PIV data. The axial turbulence intensity is somewhat higher than in the 10 kHz case, which is believed to be a result of the higher sampling frequency capturing more of the high frequency fluctuations in the flow and possible aliasing effects. This will become more apparent in the next section on spectral analysis. The data quality is nearly 100% throughout the measured flow field for the 25 kHz data set. Again the turbulence estimates in the shear layer at x/D <0.7 appear to be much higher than expected, due to the large velocity gradients in this region of the flow.

IV B. Spectral Analysis

The TR-PIV data were initially processed using the multi-pass, 6-pass simulated annealing algorithm described above, without subregion distortion. Two sample sets of data for a flow condition of Mach 0.5 cold flow (T/T_∞=0.89) are shown in figures 8a-b. Power Spectral Densities (PSD) for both 10 kHz and 25 kHz TR-PIV data are shown along with a hotwire PSD at a radial location on the nozzle lip line (y/D=-0.5) and at axial locations of x/D=2 and x/D=3. The 10 kHz TR-PIV data were processed using 512 point periodograms and the 25 kHz TR-PIV data were processed using 1024 point periodograms in order to keep the frequency bands approximately equal. In both cases a Welch window was applied to the time records. The 10 kHz hotwire data was anti-alias filtered at 4 kHz and processed using 1024 point periodograms and a Welch window. The hotwire spectra have a lower variance than the 10 kHz and 25 kHz TR-PIV spectra due to both the application of anti-alias filtering and the larger number of data segments (K=78, vs. K=60 or K=42 for TR-PIV) averaged together to compute the periodogram. The 10 kHz and 25 kHz TR-PIV data appear to exhibit higher broadband noise across the entire frequency spectrum and appear to have a "dogleg" or lift off at the high frequency end of the spectra. The TR-PIV data shown in figure 8a and 8b were then smoothed using a 5 point moving average filter, as shown in figures 8c and 8d. All of the TR-PIV data exhibited the general traits presented here, which caused concern over the data quality. The next few sections describe the steps taken to account for the features observed in the TR-PIV data and how these apparent biases were mitigated and/or removed.

The initial TR-PIV data processing strategy using standard multi-pass PIV processing appeared to be inadequate. As shown for the ensemble averaged results, utilization of the subregion distortion processing technique improved the quality of the processed data records. Application of the subregion distortion technique also yields a dramatic improvement in the PSDs as shown in figures 9a-b, again at x/D=2.0 and x/D=3.0. The broadband noise observed in the standard processing has been removed and both the 10 kHz and 25 kHz PIV data now lie more nearly on top of the hotwire spectra for the range of 1 kHz and above. Below 1 kHz there are some slight deviations between the TR-PIV data and the hotwire spectra. The high frequency dogleg is still apparent in the PIV spectra, but the severity of the lift off has been significantly reduced in both cases. The 25 kHz spectrum appears to have more energy in the lower frequency bands than the 10 kHz PIV spectra.

It is important to understand the improvements in the flow spectra obtained via the application of the subregion distortion technique. Along with mitigating velocity gradients across the subregion, the subregion distortion processing is also recognized to remove peak-locking effects in the PIV image data.[15] The flow velocity spectra presented above without subregion distortion illustrate that the time records of velocity have broadband noise across the entire record. The source of this broadband noise is attributed to peak-locking in the processed vector maps. The histograms of the u- and v-velocity components for the 25 kHz PIV data shown in figure 8d and 9b above are plotted in figure 10 for the standard PIV Processing and the subregion distortion processing cases at x/D=3. These histogram plots are at a single point in space, across the entire time record of 61440 velocity measurements. The standard PIV processing results for the u- and v-components of velocity reveal evidence of severe peak-locking, as shown in figure 10a and b. Application of the subregion distortion processing immediately mitigates the peak locking effects, yielding continuous velocity displacement histograms, as shown in figures 10c and d. The subregion distortion processing reduces the broadband noise in the TR-PIV spectra, the source of the broadband noise is shown here to be predominantly caused by peak-locking artifacts from the Standard PIV processing. Elimination of the peak-locking bias yields more accurate flow spectra and more accurate velocity estimates overall.

IV C. Aliasing

The subregion distortion processing appears to yield the best quality TR-PIV velocity vector map and flow spectra, which very closely match the hotwire spectra. However, the source of the high frequency lift off must still be determined in order to fully qualify the TR-PIV measurements. The source of the "dogleg" in the TR-PIV spectra is suspected to result from aliasing of the high frequency portion of the spectra. The aliasing of the frequency content in the flow beyond the sampling rate should manifest itself across the entire frequency range of the spectra. In actual practice, it is not possible to anti-alias filter the TR-PIV data when it is acquired, which is the standard approach when acquiring hotwire data. In order to investigate the suspected aliasing contribution, the 25 kHz data records were anti-alias filtered and then subsampled down to 12.5 kHz records and 6.25 kHz records. The length of the periodograms are decreased in direct proportion to the subsampled record length (a factor of 2 or 4) in order to keep the frequency bands equal when comparing the PSDs of the subsampled data sets.

The anti-alias filtering example is performed on the spectra from the x/D=3.0 case. A 16th order Butterworth filter was implemented in the time domain by applying a 4th order Butterworth filter in 4 passes through the time records. The direction of the filter was reversed in each pass to preserve the phase of the original signal. The anti-alias cutoff frequencies were set to 7/8 of the Nyquist frequency. The 25 kHz raw signal, the 25 kHz raw signal anti-alias filtered at 10.9 kHz and the subsampled raw 25kHz spectra at 12.5 kHz and 6.25 kHz are shown in figure 11a, where a 5 pt moving average has been applied to the spectra. The anti-alias filtering has no effect on the 25 kHz raw signal except as expected at the cutoff frequency. For the raw 25 kHz data, this is really not an anti-alias filter since the TR-PIV data are already aliased. The filtered signal is shown here to illustrate that the filtering operation does not distort the low frequency portion of the spectra and performs as expected. The subsampled data records tend to be noisier since the record length has been reduced by the subsampling factor (2 or 4). Subsampling the 25 kHz record yields aliased frequencies across the entire spectrum, as shown by the 12.5 kHz and 6.25 kHz subsampled cases. As the degree of undersampling increases, more lift off is observed at the high frequency end of the spectra and there is also a general broadband offset observed across the entire range of the spectrum. All of the spectra have the same general shape in the low frequency range of the spectrum. The 12.5 kHz data has a little more energy at the low frequency end than the 25 kHz signal – but generally matches the raw data at the mid frequencies.

Figure 11b contains the same data as 11a with the addition of the anti-alias filtered, subsampled raw 25kHz spectra at 12.5 kHz and 6.25 kHz. All of the filtered spectra (12.5 kHz subsampled, filtered at 5.5 kHz, 512 pt periodogram and 6.25 kHz subsampled, filtered at 2.7 kHz, 256 pt periodogram) lie on top of the 25 kHz raw spectra at the low frequency end of the spectrum (< 1 kHz). Only the unfiltered 12.5 kHz and 6.25 kHz data sets have higher energy in the low frequency portion of the spectrum, indicating that this energy is the result of the aliasing of higher frequencies into these low frequency bands. The filtered signals also roll off at the filter cutoff frequency illustrating that the high frequency lift off observed in all of the acquired TR-PIV data is another aliasing effect.

Additional tests were performed, which are not included here, using a white noise time record in order to confirm that subsampling the time signals results in a broadband increase in the energy in the spectrum. The observed effect was a constant offset in the spectrum energy level in direct proportion to the ratio of the subsampling. Hence the results observed here on the TR-PIV data are confirmed to be a direct consequence of aliasing effects.

Filtering the data prior to subsampling removes the dogleg at the high frequency end of the spectrum and also reduces the aliasing at low frequencies – confirming that aliasing is manifested as both low and high frequency contamination of the collected data. Although anti-alias filtering the TR-PIV data is not possible, we are now confident that we understand the characteristics of the spectra obtained using TR-PIV. Hard limits must be applied to the range of the spectra that are not contaminated by aliasing. The hard limit for the 25 kHz PIV data with subregion distortion processing is approximately 8-10 kHz. The hard-limit for the 10 kHz TR-PIV data is 3-4 kHz. The best means for minimizing the effect of aliasing is to acquire the TR-PIV data at the highest frequency possible and to employ the subregion distortion processing to remove the effect of the peak-locking on the processed spectra. It is also anticipated, that due to aliasing, the turbulence estimates obtained from the TR-PIV measurements could be slightly higher than the true values.

IV D. TR-PIV versus Hotwire

Radial surveys at the nozzle centerline were taken using a hotwire probe at axial planes from 0.2 to 10.0 diameters downstream from the nozzle exit. The hotwire probe was mounted on a horizontal translation stage within the large blue traverse rig used to translate the PIV system shown in figure 1. The surveys were obtained at y/D increments of 2.5. Figure 12a contains line profiles of the relative standard deviation in the u-component of velocity normalized by the ideally expanded jet velocity U_{id} as measured by the hotwire probe for axial locations of 0.2, 0.5, 0.7, 1.4 and 2.0 nozzle diameters. These surveys only show one-half of the nozzle radial survey plane. The relative turbulence in the axial velocity along the lip line ranges from $\sigma_u/U_{id} = 0.05$ at x/D=0.2 to $\sigma_u/U_{id} = 0.14$ at x/D=2.0. The hotwire profiles indicate that the shear layer migrates slightly away from the nozzle centerline at increasing axial locations. The 10 kHz PIV measurement results are shown in figure 12b. The TR-PIV camera was not positioned right at the exit of the nozzle in order to keep unwanted flare light from the nozzle lip from reaching the camera. Hence, only TR-PIV axial profiles of σ_u/U_{id} at y/D planes from 0.7 to 2.0 are plotted here for comparison to the hotwire measurements. The TR-PIV measurements at x/D=0.7 are slightly corrupted due to edge effects in the processed velocity vector maps. Hence, the x/D=0.7 PIV profile is slightly higher than the corresponding hotwire profile. The TR-PIV profiles are nominally at the same level or slightly higher (0.15%) than the hotwire measurements. This is not unexpected since the TR-PIV data are aliased due to the lack of an anti-aliasing filter. The TR-PIV profiles appear to be narrower than the hotwire profiles and also appear to remain relatively centered along the nozzle lip line at increasing axial locations.

The 25 kHz PIV data shown in the ensemble averaged plots and spectral plots above generally exhibited higher turbulence levels than the 10 kHz PIV data, especially in the region $x/D < 1$. The reduced field of view (640x80 pixels/camera) required in order to obtain the 25 kHz frame pair rate limited the number of correlation grid rows (n=3) in these images when processed using a final interrogation subregion size of 32x32 pixels on 16x16 pixel centers. We have reprocessed these data sets using smaller correlation subregion sizes (16x16 pixels) and higher grid densities (4x4 pixels centers, i.e. 75% oversampling), so that the high velocity gradient in the shear layer near the nozzle is more accurately resolved by the subregion distortion algorithm. Using higher grid densities also mitigates the boundary effects caused by the high velocity gradients near the nozzle (left side of the flow field).

A comparison of the original low resolution grid processed σ_u/U_{id} values in figure 7 are replotted in figure 13a along with the values obtained using the smaller subregion size and higher grid resolution processing. Only the axial range from x/D=0.5 to 2 is shown here to illustrate the details of the shear layer flow. A larger region of the flow field is shown in the higher grid resolution case since the smaller subregions enable a larger region of the flow field to be processed. In the low resolution grid case, the turbulence levels in the shear layer are contaminated by edge effects for $x/D < 1$. In the higher grid resolution processed case, the magnitude of σ_u/U_{id} for $x/D < 1$ has been significantly reduced and now very closely match the hotwire turbulence measurements and also the 10 kHz PIV results. However, there is a slight rise in the turbulence levels (0.5 to 1%) for the higher resolution grid processing case across the entire measurement region relative to the 10 kHz PIV results. Profiles of σ_u/U_{id} at x/D=0.7 through 2.0 are shown in figure 13b, which are slightly higher (0.5%) than the 10 kHz PIV results. Again the 25 kHz measurements show a narrower shear layer than the hotwire results and also that the center of the shear layer remains relatively centered on the nozzle lip line at increasing axial locations.

The improvement in the flow measurement results from using the higher grid density and a smaller subregion size on the 25 kHz data is attributed to two factors. Near the nozzle, the turbulence is low and the velocity gradient in the shear layer is very large. In this regime, using smaller subregions with a high grid density enables the subregion

distortion technique to accurately capture the velocity gradient. Since the turbulence is low, there is no significant increase in the random noise from the use of the smaller subregion. Further downstream, where the turbulence is higher in the fully mixed region of the flow, the use of smaller subregions results in more random error due to the flow turbulence and also possibly due to the mixing of the ambient smoke seeding with the core flow aluminum oxide seeding. When the two seed materials mix together, the gray haze from the smoke adds a uniform background to the flow, which reduces the contrast and yields a slightly broader correlation peak with a halo of energy around it. There may also be a general reduction in the concentration of flow seeding far from the jet due to mixing of the jet core flow with the ambient air.

Examination of the flow spectra for the high resolution grid processing case shows that the spectra are very similar to the 10 kHz case spectra for x/D < 1.4. For the range x/D >1.4 there is a slight increase in energy across the entire spectrum along with a return of the "dogleg" lift off at high frequencies. Subtracting the time records from the low resolution case from the high grid resolution case at an axial location of x/D=3 and y/D=-0.5 yields a uniformly noisy signal. The spectrum of the difference signal is flat across the entire frequency range, confirming that it is white noise. The increase in broadband noise is caused by the smaller subregion size along with a possible contribution from the degradation of the correlation peak due to the flow seeding. An optimal processing strategy would be to examine the local flow gradients versus seeding quality and adjust the correlation subregion size accordingly. Even with the limited spatial resolution of the 25 kHz measurements, by appropriately selecting the processing strategy, the large velocity gradient (164 m/s/8mm) across the jet flow shear layer is still clearly resolved.

In all of the analyses above, we have focused on the nozzle lip line. It is also constructive to compare the spectral surveys obtained using the hotwire against the TR-PIV results over the remainder of the radial extent of the flow. Figure 14a shows the hotwire survey planes plotted at three x/D planes (5, 7, 10) versus survey location y/D versus frequency in Hz. In figure 14b the 10 kHz PIV data at x/D=5 are overlaid on the hotwire data. The TR-PIV measurements very closely match the hotwire measurements in magnitude and spatial extent, both along the lip line and over the radial extent of the PIV system field of view. The agreement between the TR-PIV and the hotwire measurements are nearly identical at x/D = 7 and 10. Note that we have only shown a single line from the TR-PIV data set. The TR-PIV results contain a nearly continuous block of y/D surveys from x/D=0.5 out to x/D=6 for a singe axial measurement station. TR-PIV measurements were acquired at several overlapping axial stations, yielding a continuous 2-D map of flow spectra from x/D=0.5 to x/D=12.

In summary, the hotwire data were collected with a very conservative anti-aliasing filter cutoff frequency, which led to under-estimated turbulence levels near the nozzle. The 10 kHz TR-PIV data exactly match the hotwire results for x/D > 1, which are accurate to better than 1%. The 25 kHz TR-PIV results showed turbulence levels slightly higher (0.5-1%) than the hotwire results due to a limitation of the imaged field of view and possible flow seeding effects. Additional hotwire measurements are required at a higher sampling rate and with a higher anti-aliasing filter cutoff frequency in order to fully evaluate the 25 kHz TR-PIV results.

IV E. Two-Point Statistics

The correlation of the axial velocity in the axial direction, as defined by equation 1 defines $R_{uu}(\xi,\tau)$ as the element in the correlation tensor that we are computing. The axial velocity space-time correlations were computed at the reference locations x/D = 1 and 2 and at y/D = -0.5 for the 25 kHz TR-PIV data at the Mach 0.9 flow condition and at the temperature ratios: T/T_∞=0.89 and 1.76. Spatial shifts in the axial direction are denoted ξ_x and spatial shifts in the radial direction are denoted ξ_y. Figure 15a-d shows the axial velocity correlation $R_{uu}(\xi,\tau)$ for the two temperature ratios at the $\xi_y = 0$ plane (zero radial shift), where the vertical axis is dimensionless time lag, τ, scaled by the convective velocity U_c and the nozzle diameter and the horizontal axis is the dimensionless spatial shift ξ_x/D. The correlation function starts out at unity amplitude at zero time (τ=0) and space (ξ_x=0) shifts and then clearly delineates the decay of the turbulence in the jet flow, via the decreasing amplitude of the correlation peak and the broadening of the spatial extent of the turbulence. The slope of the correlation function is directly proportional to the convection velocity, which for the T/T_∞=0.89 case is 198 m/s and for the T/T_∞=1.76 case is 169 m/s. The reduction in the convection velocity for the hot flow case is caused by the higher momentum of the colder ambient flow, which through mixing inside the shear layer, is pulling down the amplitude of the core jet velocity. At x/D =1, the correlation length is fairly short and there appears to be no significant difference between the cold and hot cases. At x/D=2, the hot flow case shows a faster growth rate of turbulent structures, as indicated by the width of the

correlation function. The quality of the TR-PIV data records is verified by the clearly defined correlation function even at these locations very close to the jet where the turbulence structures are just beginning to develop.

V. Conclusions

Measurement of space-time correlations in both hot and cold jet flows is now possible due to the development of a Temporally Resolved PIV system. Using the TR-PIV system to capture a long (6 jet diameters) spatial extent of the nozzle shear layer provides simultaneous spatial and temporal maps of the flow field properties. Application of TR-PIV in a Mach 0.5 jet flow revealed turbulent structures which were clearly observed to advect downstream in animations of the long vector map sequences. The high quality, high spatial resolution velocity vector maps are attributed to the high quality, uniformly dispersed flow seeding and through the use of advanced PIV data processing strategies such as Symmetric Phase Only Filtering and subregion distortion.

TR-PIV time records were acquired at both 20 kHz and 50 kHz, yielding processed, planar flow measurement time records at 10 and 25 kHz. The planar velocity time records were used to compute flow spectra at all points across the processed PIV velocity vector maps. Examination of the spectral properties of the TR-PIV spectra confirmed that the PIV data were contaminated by "peak-locking" effects and aliasing. Application of the subregion distortion processing technique was shown to eliminate the peak-locking in the measured data and thereby remove the observed broadband noise in the flow spectra.

Residual aliasing in the PIV measurements due to the lack of an anti-aliasing filter was confirmed by subsampling and filtering of the 25 kHz PIV measurement records down to 12.5 kHz. In addition, studies using white noise time records and anti-alias filtering confirmed the effect of subsampling on the broadband noise content in the TR-PIV data. The best recommendation that can be made is to acquire TR-PIV at the highest temporal resolution possible. This will only minimize the effect of the aliasing – not completely remove it.

The TR-PIV spectra and turbulence estimates were then compared with those obtained using hotwire anemometry. The 10 kHz TR-PIV results exactly match the nominally 1% accurate hotwire results for $x/D > 1$. For $x/D < 1$, the TR-PIV turbulence estimates were higher than the hotwire results due to: 1) the low sampling rate (10 kHz) and very conservative anti-aliasing filter setting (4 kHz) used to acquire the hotwire data prematurely truncated the hotwire spectra resulting in under-estimated turbulence levels in the region $x/D < 1$; and 2) as a direct consequence of aliasing of higher frequencies in the flow down into the measured frequency bands in the TR-PIV data. The TR-PIV results showed a narrower shear layer and constant propagation trajectory compared to the hotwire results which showed a larger spread angle and a shear layer that propagated off of the nozzle lip line. High resolution grid processing of the 25 kHz PIV data illustrated that even for small fields of view and/or spatial resolutions; the high velocity gradients across the shear layer could be accurately resolved using TR-PIV. Validating the TR-PIV results in a Mach 0.5 cold flow against hotwire measurements establishes the credibility of the TR-PIV technique and the additional flow measurements obtained in compressible flows at elevated temperatures.

In addition to validating the TR-PIV measurements with hotwire anemometry, two-point space-time correlations were computed for the Mach 0.9 flow case at $x/D=1$ and $x/D=2$ for both hot and cold flow cases. The space-time correlations indicated that increasing the temperature appears to increase the growth rate of the turbulent structures. Much work still needs to be done to process and examine these time-resolved flow measurement records in order to accurately characterize the turbulence decay in jet flows. The results obtained from these further analyses will be used to verify/modify the current assumptions and models used in Computational AeroAcoustic (CAA) codes.

Current plans are to double the laser energy and camera resolution-bandwidth to facilitate larger field of view TR-PIV measurements at 25 kHz and reduced field of view measurements at 50 kHz. Acquiring velocity measurements at 50 kHz will hopefully mitigate any remaining aliasing of the high frequency turbulent fluctuations in the flow for the region $x/D > 1$.

VI. Acknowledgements

The author would like to thank Ray Loew and Dennis Eck for their support in the operation of the SHJAR facility and also thank W. Trevor John and Garret Clayo for their assistance in the setup and installation of the DPIV system. Discussions with Dr. James Bridges were also invaluable in interpreting some of the results.

References

1) Wernet, M. P. and Bridges, J., "Application of DPIV to Enhanced Mixing Heated Nozzle Flows," AIAA 2002-00691, 40th Aerospace Sciences Meeting, Reno, NV 2002.

2) Bridges, J. and Wernet, M. P., "Measurements of the Aeroacoustic Sound Source in Hot Jets" AIAA-2003-3130, 9th AIAA/CEAS Aeroacoustics Conference, Hilton Head, SC, 2003.

3) Lighthill, M. J., "On Sound Generated Aerodynamically, I. General theory," Proc. Royal Soc. London A, 211, 564-587, 1952.

4) Seiner, J. M., Ukeiley, L. S., Ponton, M. K., and Jansen, B.J., "Progress in Experimental Measure of Turbulent Flow for Aeroacoustics," AIAA 2002-2402, AIAA/CEAS Aeroacoustics Conference, Breckenridge, CO 2002.

5) Chu, W. T., "Turbulence Measurements Relevant to Jet Noise," Univ. Toronto Institute for Aerospace Studies, UTIAS Report 119, 1966.

6) Laurence, J. R., "Intensity, Scale, and Spectra of Turbulence in Mixing Region of Free Subsonic Jet," NACA Report 1292, 1956.

7) Ahuja, K. K., Lepicovsky, J., Tam, C.K.W., Morris, P.J., and Burrin, R.H., "Tone-Excited Jet: Theory and Experiments," NASA CR-3538, 1982.

8) Oakley, T. R., Loth, E., Adrian, R. J., "Cinematic Particle Image Velocimetry of High-Reynolds-Number Turbulent Free-Shear Layer," AIAA Journal 34(2), pp. 299-308, 1996.

9) Hu, H., Saga, T., Kobayashi, T., Taniguchi, N., Yasuki, M., "Dual-Plane Stereoscopic Particle Image Velocimetry: System Setup and its Application on a Lobed Jet Mixing Flow," *Exper. In Fluids*, **31**, pp. 277-293, 2001.

10) Wernet, M. P. and Opalski, A. B., "Development and Application of a MHz Frame Rate Digital Particle Image Velocimetry System", AIAA-2004-2184, 24th Aerodynamic Measurement Technology & Ground Testing Conference, Portland, OR, 2004.

11) Thurow, B. and Satija, A., "Design of a MHz Repetition Rate Pulse Burst Laser System at Auburn University" AIAA-2006-1384, 44th Aerospace Science Meeting, Reno, NV, 2006.

12) Bueno, P. C., Ganapathisubramani, B., Clemens, N. T., and Dolling, D. S., "Cinemagraphic Planar Imaging of a Mach 2 Shock Wave/Turbulent Boundary Layer Interaction", AIAA-2005-0441, 43rd Aerospace Sciences Meeting, Reno, NV, 2005.

13) Wernet, J. H. and Wernet, M. P., "Stabilized Alumina/Ethanol Colloidal Dispersion for Seeding High Temperature Air Flows," *Proceedings of the ASME Symposium on Laser Anemometry: Advances and Applications,* Lake Tahoe, NV, 1994.

14) Wernet, M. P., "Fuzzy Logic Enhanced Digital PIV Processing Software," *Proceedings of the 18th International Congress on Instrumentation for Aerospace Simulation Facilities (ICIASF),* Toulouse, France, June, 1999.

15) Gui, L., Werely, S.T., "A Correlation-Based Continuous Window-Shift Technique to Reduce The Peak-Locking Effect in Digital PIV Image Evaluation", *Exper. In Fluids*, **32**, pp. 506–517, 2002.

16) Westerweel, J., "Fundamentals of Digital Particle Image Velocimetry", *Meas. Sci. Technol.*, **8,** pp. 1379-1392, 1997

17) Taylor, J. R., An Introduction to Error Analysis, University Science Books, Oxford University Press, Mill Valley, CA., 1982.

18) Welch, P. D., *Modern Spectrum Analysis* (New York: IEEE Press), Childers, D.G. (ed.), 1978

19) Wernet, M. P., "Symmetric Phase Only Filtering: a New Paradigm for DPIV Data Processing", *Meas. Sci. Technology*, **16**, pp. 601-618, 2005.

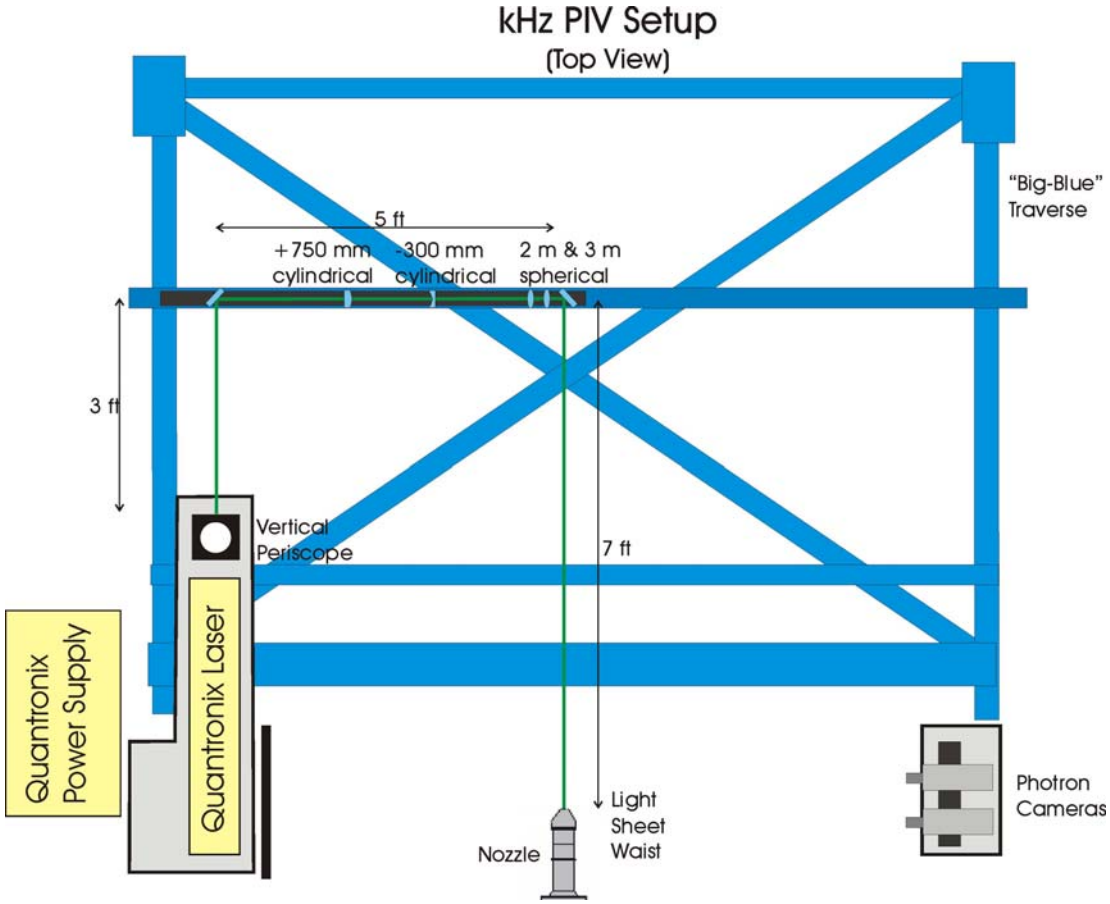

Figure 1: Schematic layout of kHz PIV system in the Small Hot Jet Acoustic Rig.

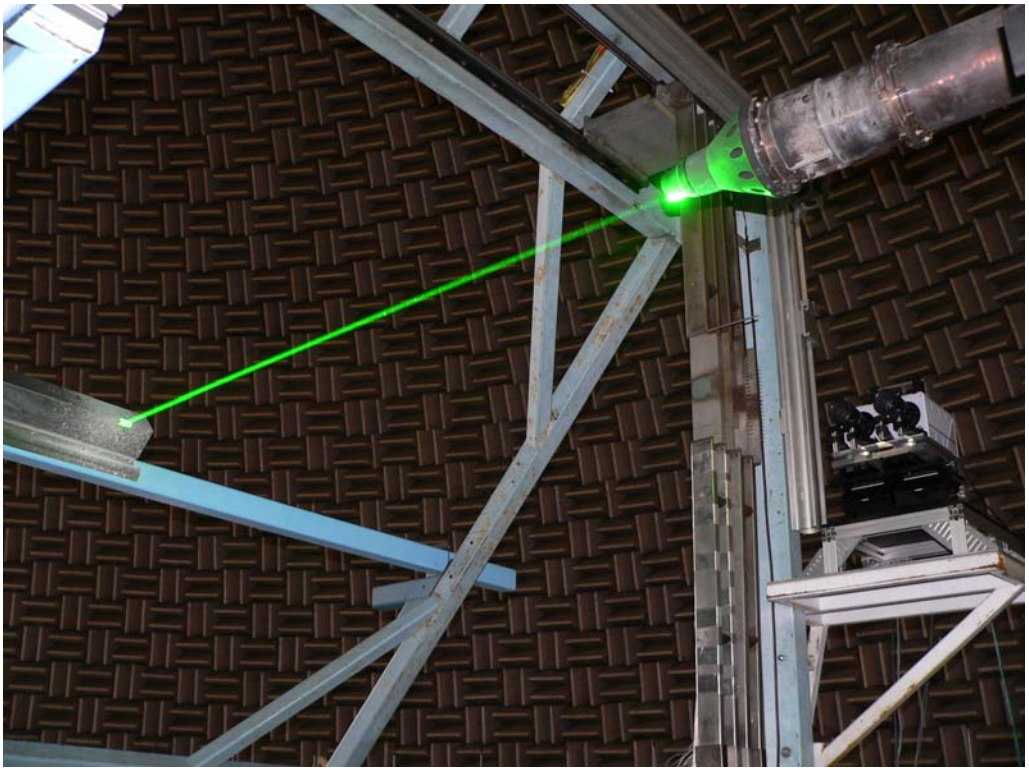

Figure 2: Picture of the setup in the SHJAR facility showing the cover over the light sheet forming optics, the light sheet impinging on the nozzle lip and the two Photron cameras.

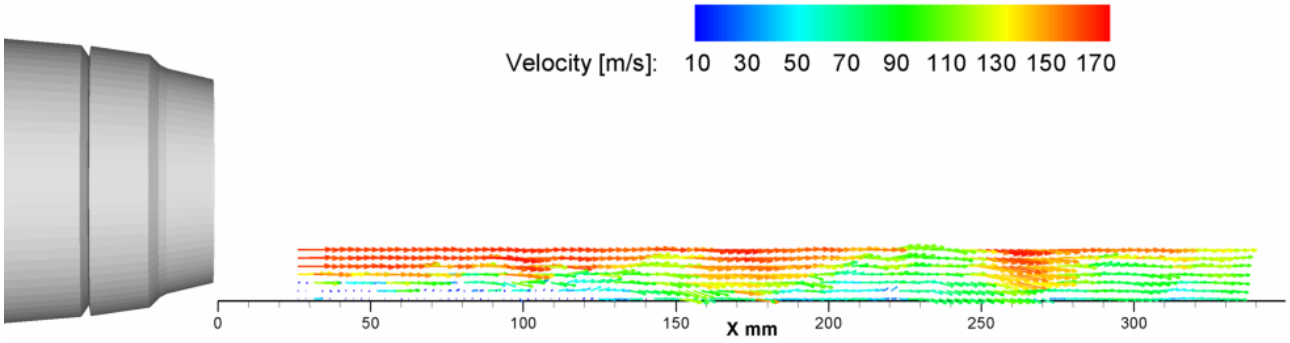

Figure 3: A single velocity vector map from the 10 kHz PIV setup which illustrates the location of the measurements relative to the nozzle and the spatial resolution of the results.

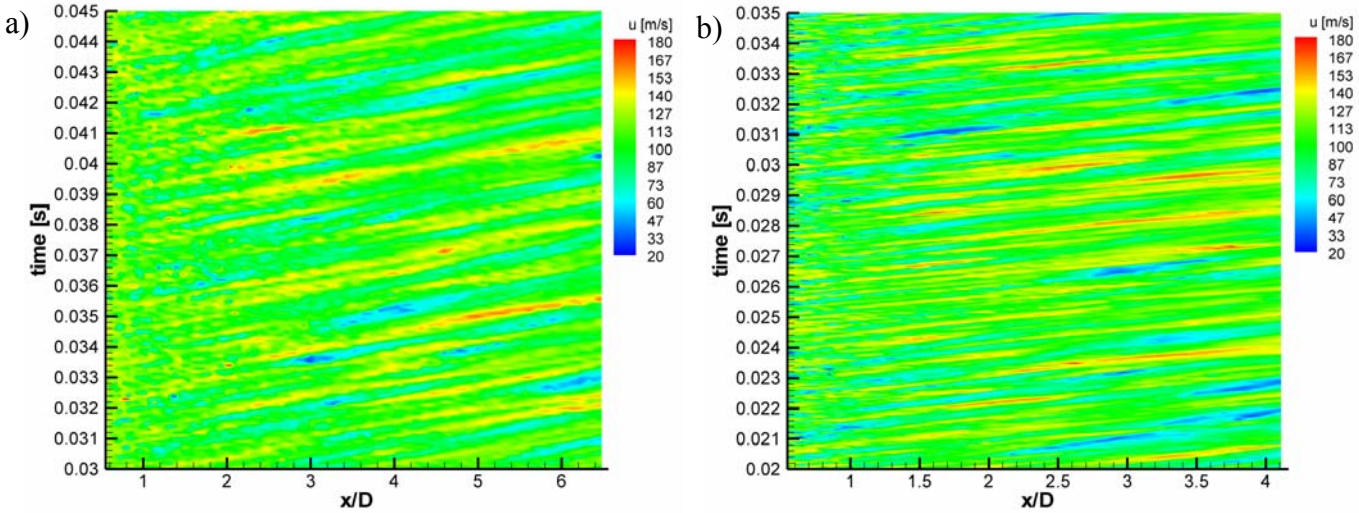

Figure 4: Plots of the u-component of velocity along the nozzle lip line as a function of axial position versus time: a) 10 kHz PIV, b) 25 kHz PIV.

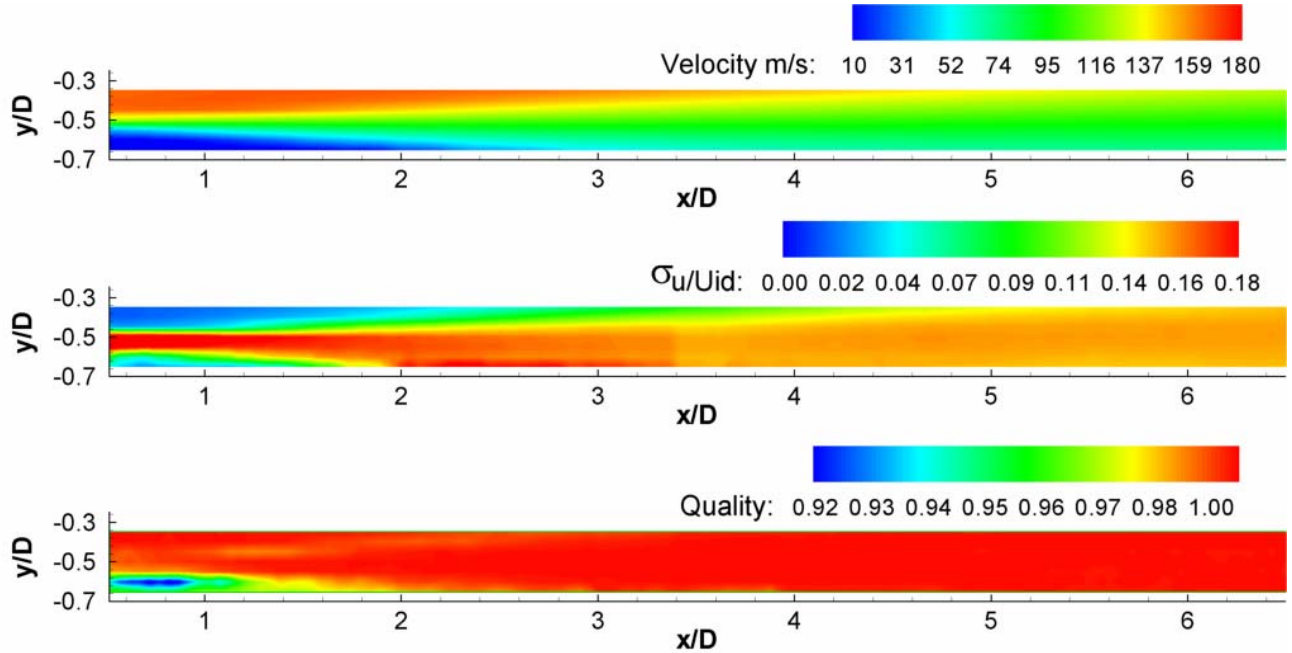

Figure 5: Ensemble averaged flow field showing velocity, σ_u/U_{id} and data quality for the 10 kHz PIV case with the left and right camera views merged. Note the loss of quality in the lower left portion of the flow due to the light sheet edge.

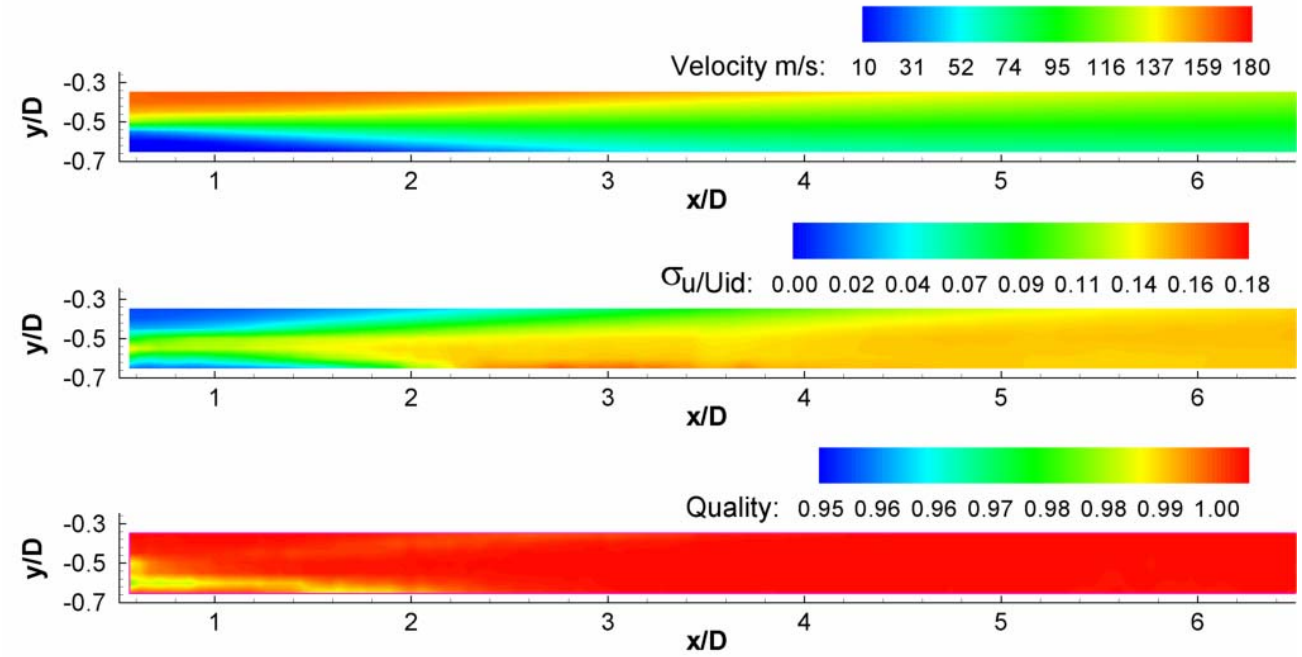

Figure 6: Ensemble averaged flow field showing velocity, σ_u/U_{id} and data quality for the 10 kHz PIV using Symmetric Phase Only Filtering and subregion distortion processing. The effect of the light sheet edge on the quality in bottom left of the flow field is greatly diminished and the turbulence levels in the shear layer are also significantly reduced.

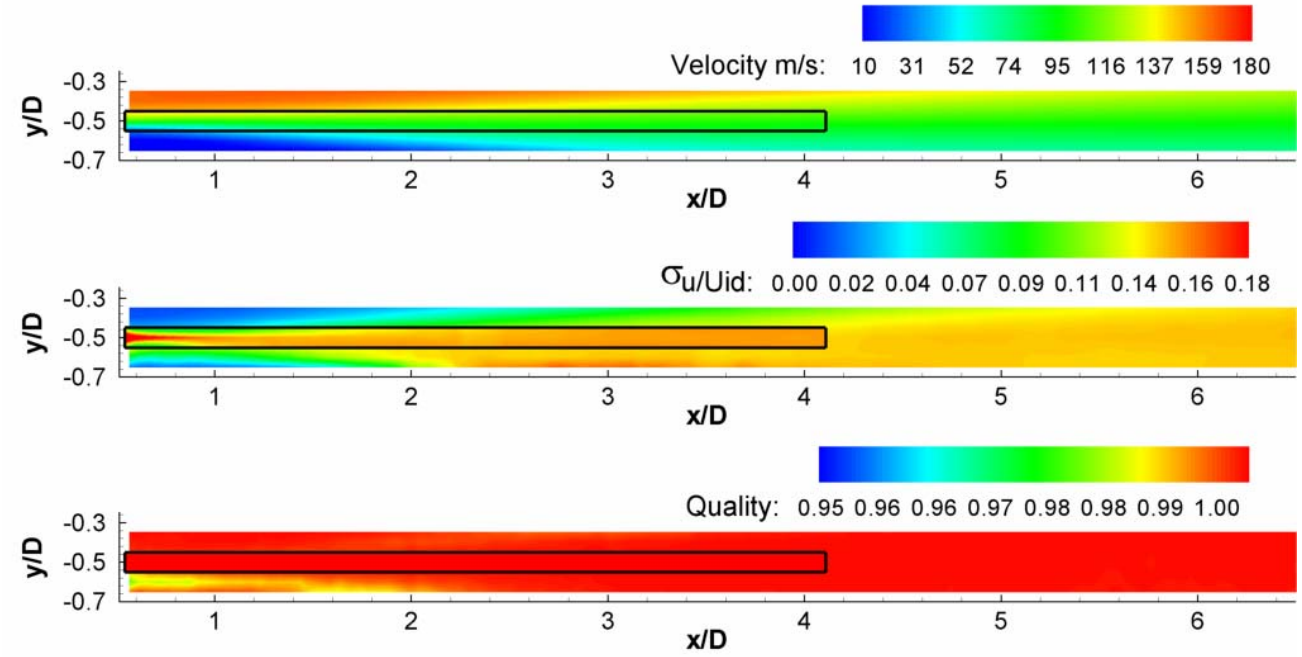

Figure 7: Ensemble averaged flow field showing velocity, σ_u/U_{id} and data quality for the 25 kHz PIV results overlaid on top of the 10 kHz case. The black outline denotes the extent of the 25 kHz measurements. The quality of the 25 kHz data is high across the entire measurement region. The turbulence intensities are higher than the 10 kHz result shown in figure 6, which is believed to be the result of the higher sampling frequency capturing more of the high frequency content in the flow.

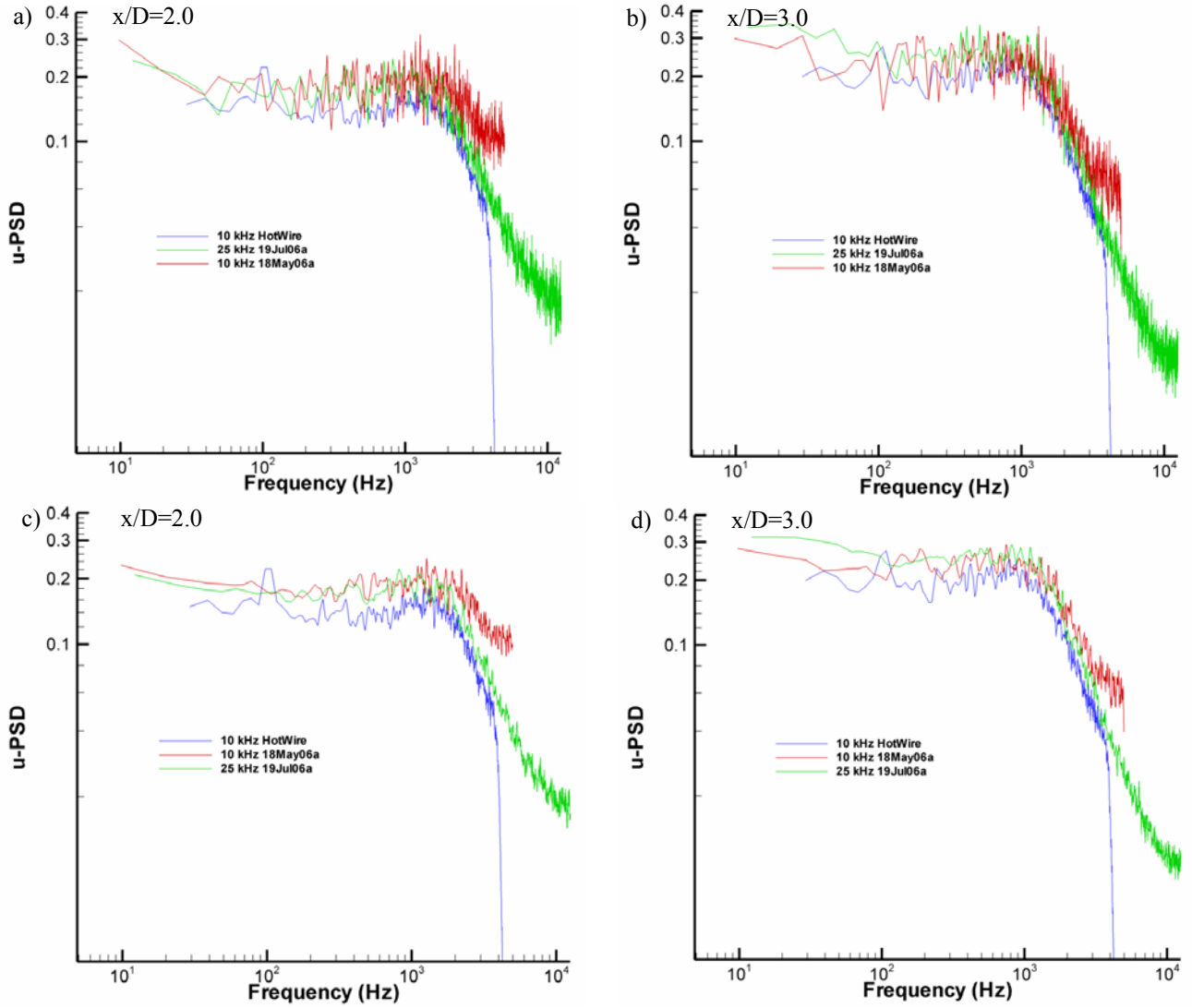

Figure 8: Comparison of Standard Processing PIV with hotwire spectra for :a) x/D=2, no smoothing; b) x/D=3, no smoothing; c) x/D=2, 5-point moving average; d) x/D=3, 5-point moving average.

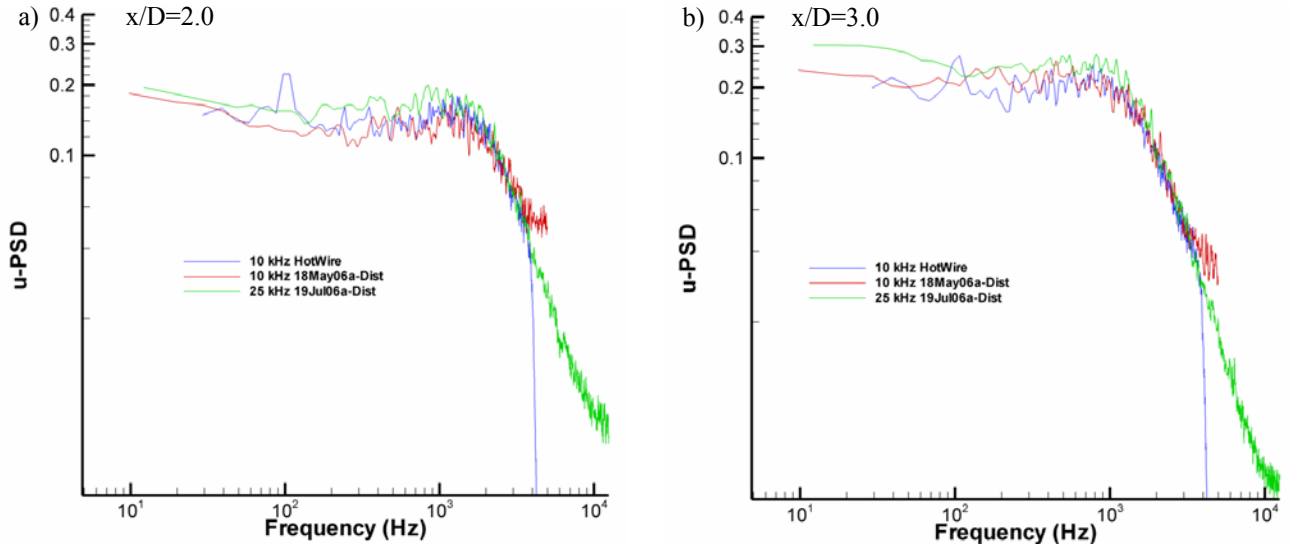

Figure 9: Comparison of Subregion Distortion Processed PIV with hotwire spectra for :a) x/D=2, 5-point moving average; b) x/D=3, 5-point moving average.

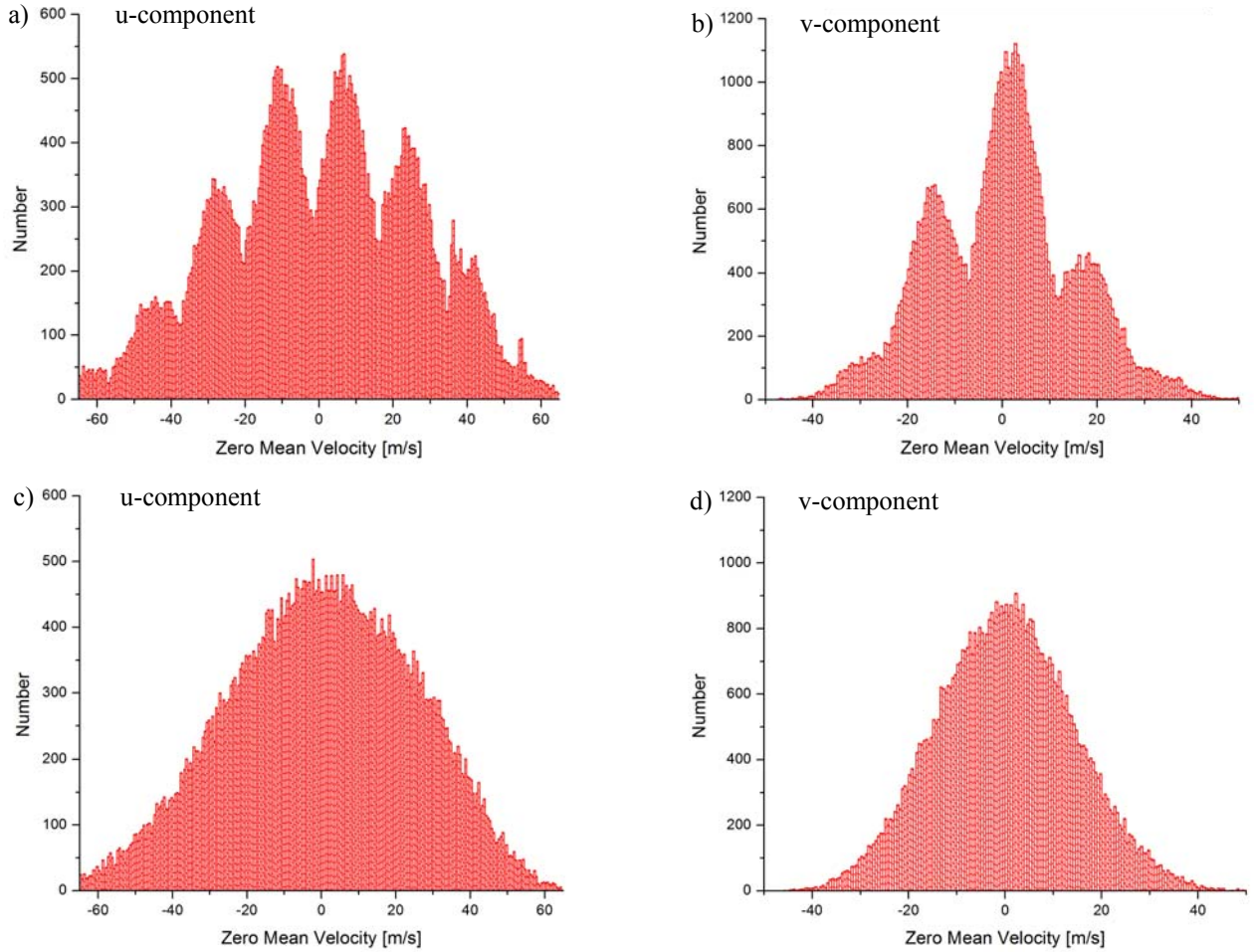

Figure 10: Probability Density Functions for a single point in the 25 kHz processed velocity vector map illustrating the "peak-locking" error caused by standard PIV processing (cases a and b) and mitigation of the peak-locking by use of subregion distortion processing (cases c and d). The pdf's are built from the time record of 61440 points at a single grid point.

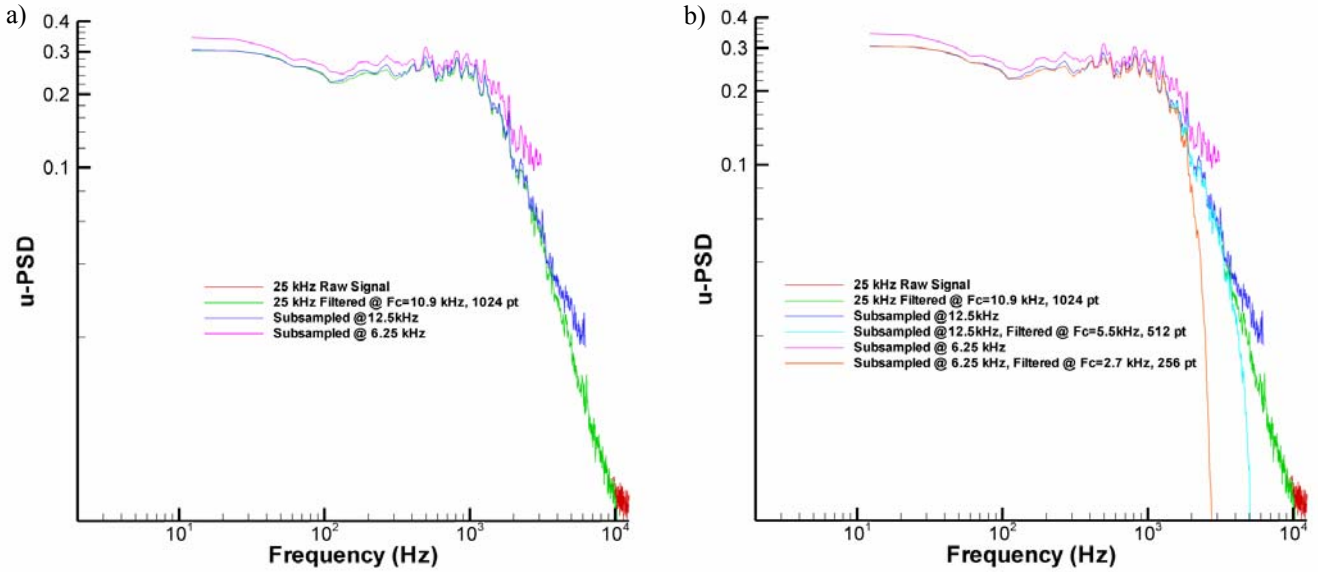

Figure 11: Effect of subsampling and filtering the 25 kHz raw signal at 12.5 kHz and 6.25 kHz: a) subsampling without filtering, the more undersampled the signals, the more energy gets aliased across the spectrum; b) subsampling with anti-alias filtering, the filtered signals now lie on top of the raw signal in the range < 1 kHz, illustrating that the anti-alias filtering removes the broadband noise across the spectra – and also truncates the signals at the cutoff frequency.

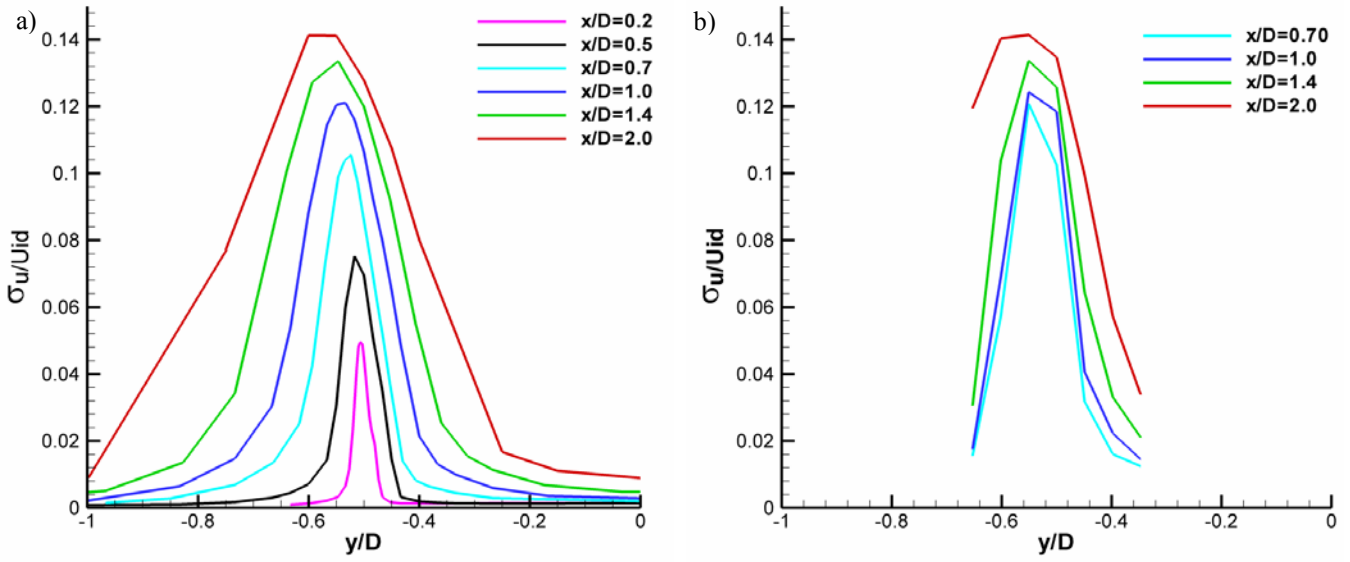

Figure 12: a) Hotwire surveys of σ_u/U_{id} at increasing axial distance from the nozzle; b) 10 kHz PIV profiles of σ_u/U_{id} which are narrower than the hotwire profiles and remain centered on the nozzle lip line.

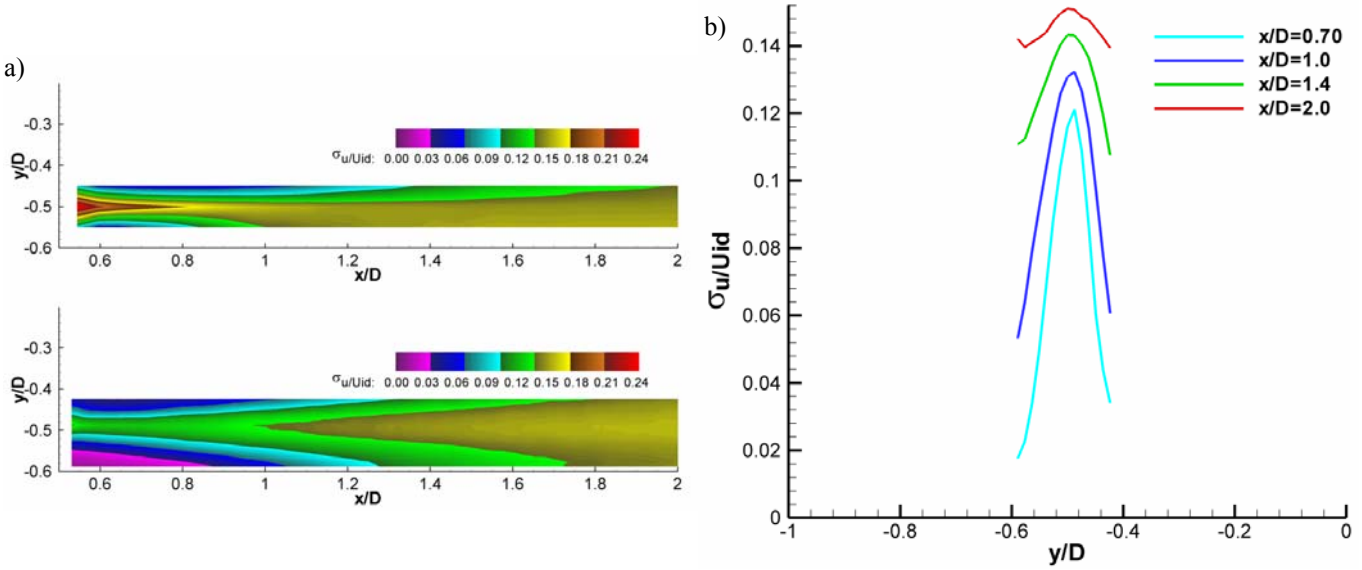

Figure 13: a) Comparison of the 25 kHz axial turbulence intensity for the low resolution processing grid (top) and high resolution processing grid (bottom), where the high resolution grid processing captures a larger region of the flow field; b) 25 kHz PIV profiles of σ_u/U_{id} which are narrower than the hotwire profiles and remain centered on the nozzle lip line.

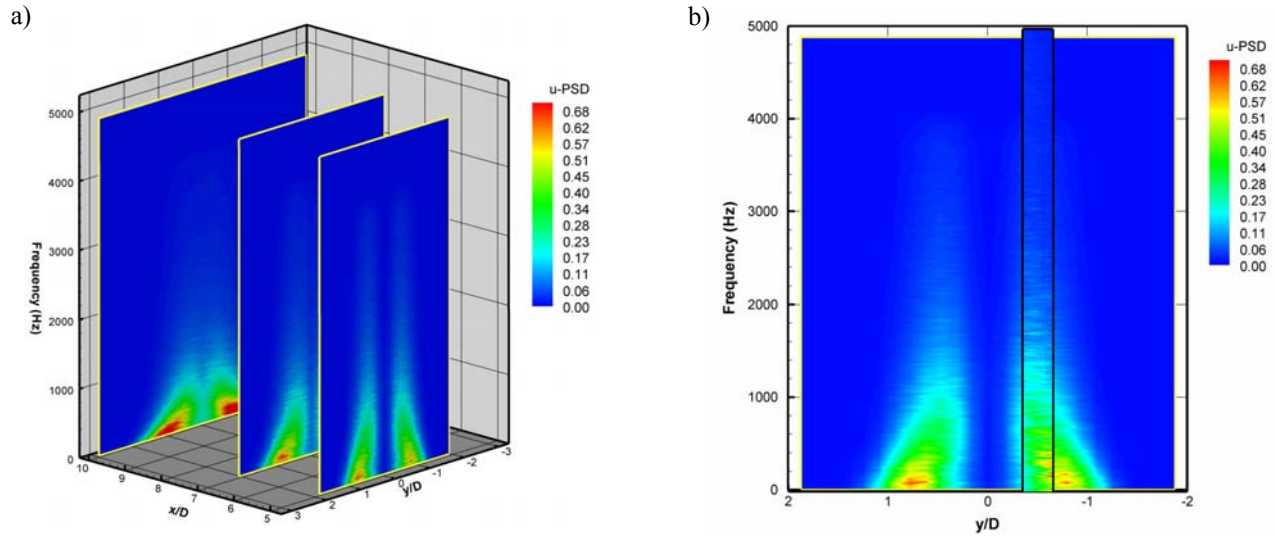

Figure 14: a) Hotwire radial surveys showing computed spectra; b) TR-PIV results overlaid on hotwire survey at x/D=5. The TR-PIV results very closely match the hotwire results even off of the nozzle lip line at x/D=5 and at survey planes further downstream.

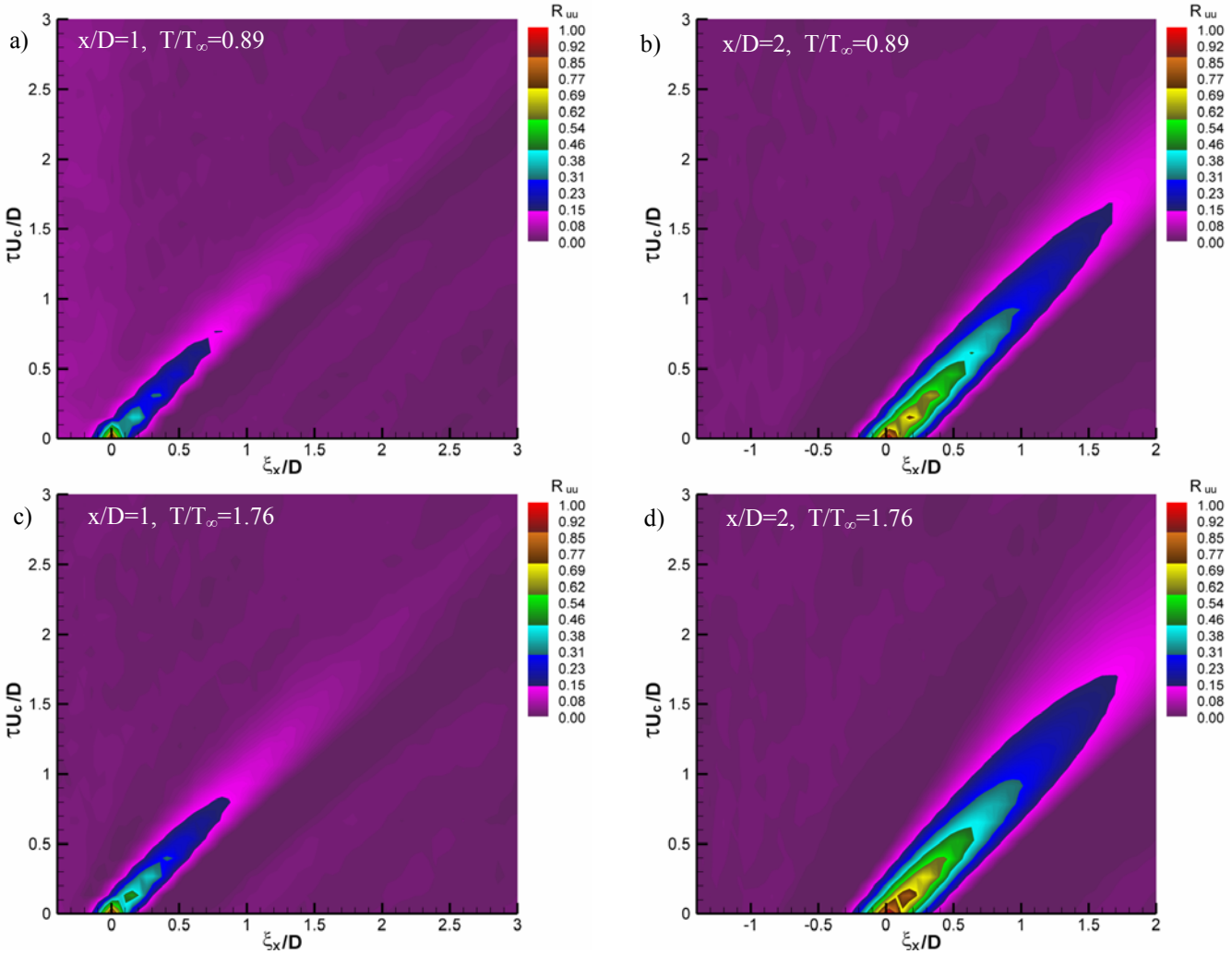

Figure 15: Space-Time correlations R_{uu} computed at x/D =1 & 2 and y/D=-0.5 for the Mach 0.9 flow case: a) and b) cold flow: T/T_∞=0.89; c) and d) hot flow: T/T_∞=1.76. At x/D=1, the correlations start at unity and decrease very quickly and spreads out due to the flow turbulence. For the hot flow cases the convective velocity is slightly lower and the correlation lengths are longer than the cold flow case. At x/D=2, the turbulent structures are growing as they convect downstream - as indicated by the wider spread in the correlation function.